Supporting Information

Hydrogen Evolution Activity Tuning via Two-Dimensional Electron Accumulation at Buried Interfaces

Yudong Xue,[a,b,c,d*] Zachary S. Fishman,[a,c] Yunting Wang,[e] Zhenhua Pan,[a,c] Xin Shen,[a,c] Rito Yanagi,[a,c] Gregory S. Hutchings,[a] Mingzhao Liu,[f] Shili Zheng,[b] Yi Zhang,[b] Eric I. Altman,[a] and Shu Hu[a,c*]

[a] Department of Chemical and Environmental Engineering, Yale University, New Haven, Connecticut 06511, United States

[b] National Engineering Laboratory for Hydrometallurgical Cleaner Production Technology, CAS Key Laboratory of Green Process and Engineering, Institute of Process Engineering, Chinese Academy of Sciences, Beijing 100190, China

[c] Energy Sciences Institute, Yale University, West Haven, Connecticut 06516, United States

[d] University of Chinese Academy of Sciences, Beijing 100049, China

[e] School of Chemical and Environmental Engineering, China University of Mining and Technology (Beijing), Beijing 100083, China

[f] Center for Functional Nanomaterials, Brookhaven National Laboratory, Upton, New York 11973, United States

Table of Contents

I. Experimental Section

$Fe(NO_3)_3 \cdot 9H_2O$ (99.99 wt%), $Ni(NO_3)_2 \cdot 6H_2O$ (99 wt%), $CO(NH_2)_2$ (99.8 wt%) and $Na_2S \cdot 9H_2O$ (98 wt%) were purchased from Sigma-Aldrich and were used as received. Ni foam (NF, 99.8%, 1.5 mm thick) plates were purchased from Taiyuan Lizhiyuan Battery. Fluorine-doped tin oxide (FTO) substrates (TEC15) and fused silica (7525-03) were purchased from Hartford Glass Co. and G. M. Associates, Inc., respectively. All solutions were prepared using deionized water (DI water, 18 MΩ·cm) obtained from a Millipore deionized water system. Before coating of the NiFe bimetallic sulfides (NiFeS) nanosheets, the NiFe-layered double hydroxide (NiFe-LDH) nanosheets were grown on the NF (1 cm × 1.5 cm) during their synthesis following the method reported previously.[1] The NiFeS on the NF was synthesized by a hydrothermal sulfuration process. The NiFe-LDH/NF was put into 80 mL 0.2 mol L^{-1} Na_2S solution in a 100 mL Teflon-lined stainless-steel autoclave and then heated at 100 ^oC for 8 hours. After cooling to room temperature, the electrode was washed with water and subsequently dried in vacuum at 50 ^oC. After weighing the total mass of the

film before and after the hydrothermal process, a mass-loading of 1 mg cm^{-2} was achieved for the NiFeS/NF electrode.

TiO_2 was deposited on the top surface of the NiFeS/NF sample by atomic layer deposition (ALD). ALD growth of TiO_2 was performed using an Ultratech Fiji G2a ALD system. Tetrakisdimethylamido-titanium (TDMAT, Sigma Aldrich, 99.999%) was used as the Ti precursor. The ALD chamber was set at 150 ^oC during the growth. One TiO_2 deposition cycle consisted of a 0.06 s pulse of H_2O, 15 s pause, followed by one 0.25 s pulse of TDMAT (the precursor temperature held at 75 ^oC) and 15 s pause. The growth rate is 0.047 nm/cycle, according to our recent study.[2] The pressure diagram of the ALD process showed a typical excess amount of precursors, as shown in Figure S1, further supporting conformal coating of the TiO_2 layer. ALD pulse sequences were recorded by monitoring the reactor pressure as a function of time. TDMAT and H_2O were used as the precursor and the co-reactants, respectively, for ALD TiO_2 growth.

The deposited thickness varied at 1, 2, 5, 7, and 10 nm, which was achieved by 22, 43, 106, 149, and 213 ALD cycles. The FTO and quartz substrates were also used as a TiO_2 growth substrate for X-ray photoelectron spectroscopy (XPS) and X-ray absorption spectroscopy (XAS) characterizations, respectively.

The electrochemical measurements were carried out using a Bio-Logic SP-200 potentiostat in a three-electrode cell. Linear sweep voltammetry (LSV), with a scan rate of 2 mV s^{-1}, was taken in a 1 M KOH (aq) electrolyte. The standard deviations of overpotentials were calculated by testing the electrodes 5 times. The standard

deviations of the measured overpotentials were ± 5 mV. A carbon rod and a Hg/HgO electrode were used as the counter electrode and the reference electrode, respectively. Electrochemical impedance spectroscopy (EIS) was measured in the same cell at an overpotential of 100 mV from 10^5 to 10^{-1} Hz. The stability test was carried out using a chronopotentiometry technique at a current density of 10 mA cm^{-2}. A Hitachi SU8230 UHR cold field emission scanning electron microscopy (SEM) and an FEI Tecnai Osiris high-resolution transmission electron microscopy (HRTEM) equipped with energy-dispersive X-ray spectroscopy (EDX) were used for studying the surface morphology and elemental distribution. For transmission electron microscopy (TEM), a fragment of the sample was carefully exfoliated from the NF electrode. High-angle annular dark-field scanning transmission electron microscopy (HAADF-STEM) was used for elemental mapping characterization. X-ray diffraction (XRD) patterns were collected from a Rigaku SmartLab X-Ray diffractometer by using a Cu Kα source. The chemical states of Ni, Fe, S, Ti, and O were measured by XPS (PHI Versa Probe II) equipped with a monochromated Al source, with C 1s (assigned to the binding energy (BE) of 284.6 eV) as a calibration reference. In addition to the XPS measurements probing the orbital energies, valence band XPS was performed using a pass energy of 11.75 eV. The XAS characterization was carried out at Beamline 8-ID, National Synchrotron Light Source II (NSLS II), Brookhaven National Laboratory (BNL). A Si(111) monochromator and a Lytle detector were used for Ti K-edge absorption scanning. The XAS data analysis was performed on an Athena software package. The dissolution of Ni and Fe was determined by using inductively coupled

plasma-mass spectrometry (ICP-MS, Model iCAP Qc, Thermo Scientific). The detection limit of Ni and Fe is 0.002 μg L^{-1}. The turnover frequency (TOF) value was calculated as follows:[1, 3]

$$\mathrm{TOF} = jS/2nF \quad \text{(S1)}$$

$$n = S/(M \cdot S_{ECSA}) \quad \text{(S2)}$$

where j is the measured current density (at η = 100 mV), S is the geometric area of the electrode, 2 is the electron transfer number, n is the moles of active sites based on the electrochemical surface area (ECSA),[4] and F is the Faradic constant (96485 C mol^{-1}). Equation S2 is used to calculate n (mol) by assuming 1 mol active sites per mol of NiFeS catalysts, where S is the geometric area of the electrode, S_{ECSA} is the electrochemical surface area (m^2 g^{-1}), and M is the molar mass of the electrocatalysts (313 g mol^{-1} for the measured composition of $Ni_{1.31}Fe_{1.70}S_2$, see Supplementary Discussion).

The Faradaic efficiency of hydrogen evolution on the TiO_2/NiFeS electrodes was quantified by comparing the amount of hydrogen evolved to that of a standard Pt/C electrode of known 100% Faradaic efficiency. The concentration of hydrogen was measured using a hydrogen probe (H_2-NP, Unisense). The H_2 probe was applied in a reaction tank containing a three-electrode system. The electrode system was set in a chronoamperometry mode at a current density of 10 mA cm^{-2}.

The H^+ and OH^- permeability tests of the ALD TiO_2 membrane were performed; its schematic is shown in Figure S13. 5-nm TiO_2 was deposited onto the TEM grids (TED PELLA, INC.). A 0.25 mm × 0.25 mm window with 15 nm hydrophilic silicon

nitride membrane originally covered the hole. In preparation for the TiO_2 membrane, ALD TiO_2 was first grown over the entire surface of the silicon nitride membrane, which was subsequently etched by using a hot, concentrated NaOH solution (9 M, 80 ^oC). In the present device, the right and left compartments of equal volume are designated the retentate chamber with pH 12 (alkaline) or pH 2 (acidic) solutions and the permeate chamber with deionized water, respectively. If there is a hole, the solution will mix completely and the concentration of H^+/OH^- in the permeate chamber will be approximately 0.005 mol L^{-1}. The pH values at both sides of the membrane were tested by a pH meter (Mettler Toledo).

II. Supplementary Characterizations

As shown in Figure 1, three evident diffraction peaks, located at 44.3^o, 51.8^o, and 76.5^o, correspond to the (111), (200), and (220) crystal planes of pure Ni foam (PDF No. 00-070-0989), respectively.[5]

Electrochemical surface area (ECSA) was calculated based on its double-layer capacitance. To quantify this, cyclic voltammetry (CV) curves at different scan rates were collected in a non-Faradaic potential region (Figure S3c). The difference between the cathodic and anodic current density at 1.14 V (vs. RHE) was then plotted against the scan rates. Fitting the data discloses a good linear correlation with a slope of 22.5 mF cm^{-2} (Figure S3d). By assuming a generic specific capacitance value of 40 μF cm^{-2} in alkaline electrolytes,[4] we estimate the ECSA of 5-nm TiO_2/NiFeS and NiFeS to be 56.3 and 45.8 m^2 g^{-1}, respectively.

As shown in Figure S4, the EIS analysis indicated that NiFeS exhibited more than three times lower charge-transfer resistance (R_{ct}, 1.563 Ω) than that of the as-synthesized NiFe-LDH (5.249 Ω), indicating a dramatic decrease of resistivity after the hydrothermal sulfuration process; this also shows that the 2D NiFeS nanosheets present a higher electron transfer rate than that of NiFe-LDH nanosheet. Moreover, after 5-nm amorphous and porous TiO_2 was deposited onto the sulfides surface, the charge-transfer resistance of the nanocomposite is also decreased.

III. Supplementary Discussion

In Figure 2a, the current densities show significant variation when the value is higher than 50 mA cm^{-2}. Too high current densities and slow mass transport can cause current fluctuations, shown as spikes in Figure 2a. We chose a reasonable scan rate of 1 mV s^{-1} so that mass-transport effect is minimal. This phenomenon is affected by the Ni foam pores, as the reactant and product mass transport in-and-out of Ni foam pores. Besides, the protons and atomic H that transport through thin porous TiO_2 coatings also affects mass transport.

The samples for XPS characterizations are grounded by a metal cover on the sample stage. The XPS survey spectrum of 5-nm ALD TiO_2/NiFeS, as shown in Figure S9a, confirmed the presence of Ni, Fe, and S on the sample surface. The composition ratio of Ni and Fe is 1:1.29. The iron atom is considered a substitute doping state in the Ni_3S_2 structure.[6] The NiFe bimetallic sulfide can be written as $Ni_{3-x}Fe_xS_2$, which is abbreviated as NiFeS. In terms of the above information, we calculated and found the chemical formula of NiFeS to be $Ni_{1.31}Fe_{1.70}S_2$ or

$NiFe_{1.29}S_{1.53}$.

To determine the valance state of Ti, as-synthesized ALD TiO_2 was used for comparison. As shown in Figure 4a, the fitting results indicated that Ti in TiO_2 was predominantly in the +4 oxidation state for both as-synthesized ALD TiO_2 and TiO_2/NiFeS nanocomposites. Ti^{3+} is also present in both samples but as a small shoulder peak in the XPS spectra.[7]

The O 1s XPS peaks were deconvoluted as shown in Figure 4b. For the TiO_2/NiFeS sample, the binding energy at 529.7 and 531.1 eV correspond to the characteristic peak of Ti-O band and Ti-OH, respectively.[7] The XPS spectra of Ni 2p, Fe 2p, and S 2p were curve-fitted as shown in Figures 4c, 4d, and 4e. Their binding energies of 855.5, 712.2, and 161.8 eV for TiO_2/NiFeS were attributed to the Ni^{2+}, Fe^{3+}, and metal-S (M-S) bond, respectively. These valance states are comparable to those measured for the as-synthesized NiFeS sample.

The sampling depth of XPS is typically a few nanometers (ca. 5 nm), and when a thin coating is employed, shifts in the core-level (CL) binding energy and the valence-band maxima (VBM) can be monitored for both the substrate and the coating. CL XPS spectra were applied to understand the electronic interaction between TiO_2 and the NiFeS nanosheet. Energy shifts for the VBM due to band bending of the substrate or the coating are reflected in the shifts of their respective CL binding energy.

The Fermi level of NiFeS nanosheets was found to be shifted by upward 0.5 eV with respect to the heterojunction interface due to the effect of TiO_2 coating: due to electron donating, the binding energies of Ni $2p_{3/2}$, Fe $2p_{3/2}$, and metal-S (M-S) peak

positions at the TiO_2/NiFeS interfaces (855.5 eV, 712.1 eV, and 161.8 eV) were 0.5 eV higher than those of the as-synthesized NiFeS (855.0 eV, 711.6 eV, and 161.3 eV). Therefore, the characterization of NiFeS XPS again confirms that the electronic properties of NiFeS were tuned via the covalent coordination and electronic interaction between NiFeS nanosheets and ALD-grown TiO_2. This evidence again verified that the electrons accumulated at the interfaces of the TiO_2/NiFeS heterojunctions.

When deposited on NiFeS, TiO_2's Ti 2p and O 1s core-level shifted together by the same amount, i.e., -0.2 eV with respect to the Fermi level of NiFeS/TiO_2 heterojunctions. In the meantime, Ni 2p and Fe 2p peaks shifted together by the same amount, i.e., +0.5 eV with respect to the Fermi level of NiFeS/TiO_2 heterojunctions. Figure S9b shows the valence edge position of TiO_2 films on FTO substrates (2.94 eV BE), indicating a Fermi level that is ca. 0.4 eV below the TiO_2 conduction band edge (TiO_2 band gap of 3.34 eV). The valence edge position (2.95 eV BE) of TiO_2 on NiFeS (Figure S9c) is the same as the TiO_2 film on FTO substrates, indicating that the overcoating process did not vary the Fermi level of TiO_2 films. This observation further confirmed the formation of a heterojunction, and so the relative shifts for Ti 2p, Ni 2p, and Fe 2p core-level peaks can be used to draw the band bending diagram at the NiFeS/TiO_2 interface. As shown in Figure 5a, the band offset between NiFeS charge-transport bands and TiO_2 conduction bands at the heterojunction interface is constructed according to the relative core-level shift. What matters is the actual core-level energy shift for Ti 2p peaks when TiO_2 is an overlayer, as compared to when

TiO_2 is a bulk film deposited on FTO substrates. Compare to bulk TiO_2 at flat band, the band edge for TiO_2 overlayers shift downwards by ~ 0.2 eV; the -0.2 eV Ti 2p core-level shift indicates upward band bending of the TiO_2 overlayer at the heterojunction interface, which is consistent with n-type doping and oxygen vacancies in amorphous ALD TiO_2.[8] Compared to NiFeS bulk, the band edge of NiFeS at the interface shifts downwards by ~ 0.5 eV. Therefore, the band diagram in Figure 5a was constructed.

As shown in Figure S14b, the pH value of the right-side remains above pH 6, which affirms that the unmodified Si_3N_4 membrane on the window of the TEM grid blocks the proton transfer. With 5-nm TiO_2 covering the window, the pH in the right-side compartment decreases to 3.0, indicating that the 5-nm TiO_2 membrane presents considerable proton permeation properties.

Without the TiO_2 membrane, the equal volume solutions of two chambers mixed completely. The concentration of H^+ is expected to be 0.005 mol L^{-1} in both the retentate and the permeate compartments. The pH measurement without the TiO_2 membrane is consistent with the above calculation as the pH reached 2.3 after equilibrium. With a TiO_2 membrane applied, the pH of the water was found to increase to 3.0 ($[H^+]$ = 0.001 mol L^{-1}). After 20% H^+ transfer from the original acidic side of the membrane to the neutral side, excess amounts of SO_4^{2-} and H^+ will accumulate on the retentate and permeate side of the membrane, respectively. An internal electric field will form across the membrane, inhibiting the protons (i.e., H^+ or H_3O^+ ions) from passing through the membrane. Combined with the discussion for

OH^- permeation in the main text, ALD TiO_2 is favorable for the transport of H^+ as well as water and an OH^- species of slightly larger Van der Walls radius, all of which participate in alkaline HER. The protons produced during water dissociation will transfer through the coating to the TiO_2/NiFeS interface. Then the H^+ and OH^- ions may recombine to become water molecules at the confined TiO_2/NiFeS interface.

At much higher current densities (above 200 mA cm^{-2}), the long-term stability of TiO_2 coated NiFeS catalyst was significantly affected. This observation further supported our buried interface hypothesis. Despite unfavorable conditions for high rate HER by using this TiO_2 coating with the present porosity and thickness properties, we have shown a pathway to high rate HER by improving the permeability of TiO_2 layers while keeping the electronic tuning effect.

IV. Supplementary Figures and Tables

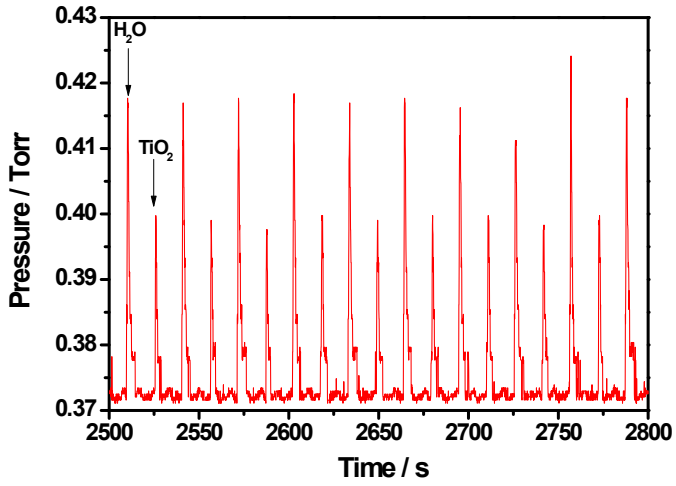

Figure S1. Recorded ALD pulse sequences by monitoring the reactor pressure as a function of time. TDMAT and H_2O were used as the precursor and the co-reactants, respectively, for ALD TiO_2 growth.

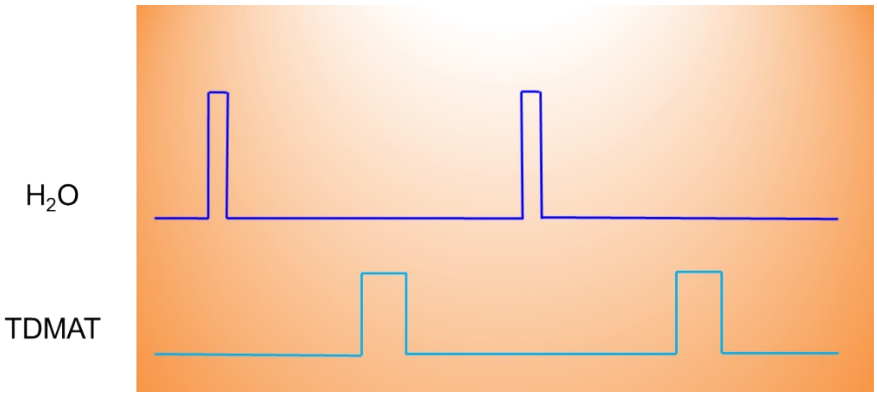

Figure S2. Schematics for the ALD precursor flow sequence, including water and TDMAT, during ALD TiO_2 growth.

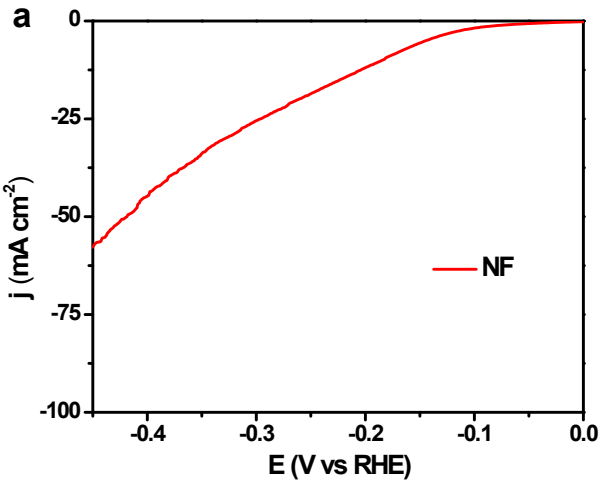
a
0
-25
-50
-75
-100
j (mA cm-2)
NF
-0.4
-0.3
-0.2
-0.1
0.0
E (V vs RHE)

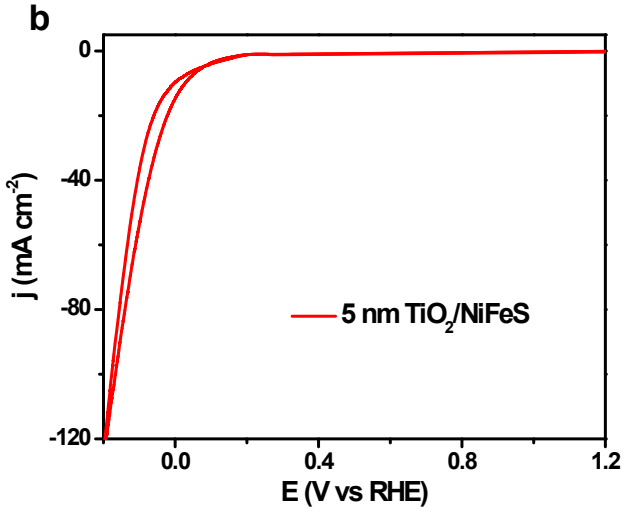
b
0
-40
-80
-120
j (mA cm-2)
5 nm TiO2/NiFeS
0.0
0.4
0.8
1.2
E (V vs RHE)

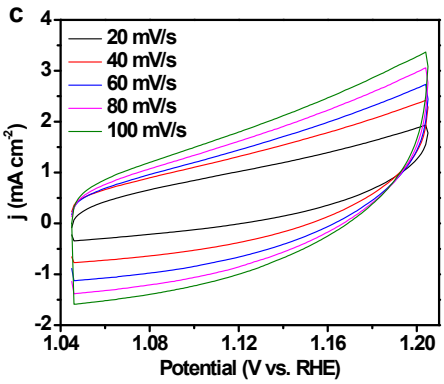
c
20 mV/s
40 mV/s
60 mV/s
80 mV/s
100 mV/s
j (mA cm-2)
1.04
1.08
1.12
1.16
1.20
Potential (V vs. RHE)

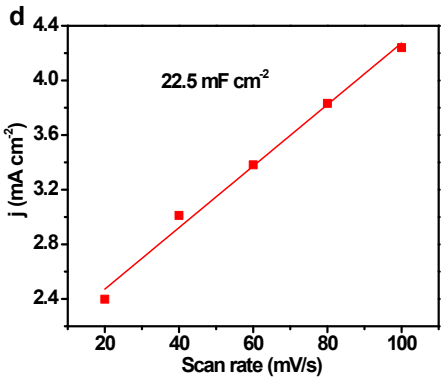
d
22.5 mF cm-2
j (mA cm-2)
20
40
60
80
100
Scan rate (mV/s)

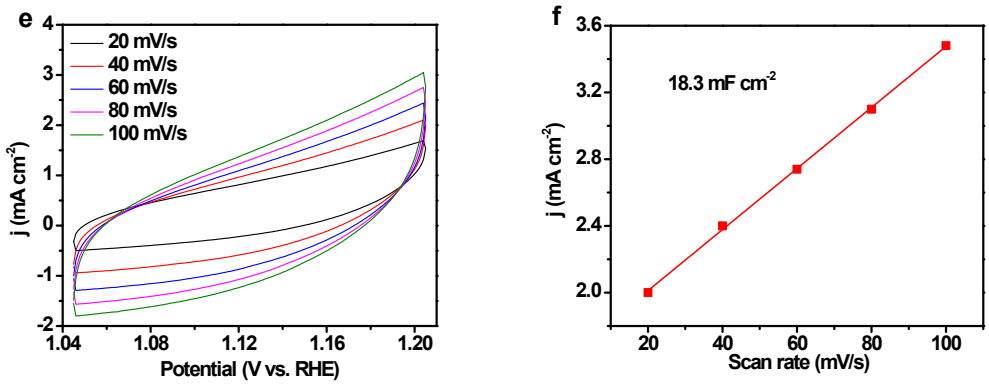

Figure S3. (a) Linear sweep voltammetry (LSV) curve of nickel foam (NF) electrode measured in a 1 M KOH (aq) solution. The overpotential at -50 mA cm^{-2} was -410 mV. (b) Cyclic voltammetry (CV) curve of the 5-nm TiO_2/NiFeS sample measured in a 1 M KOH (aq) solution. (c) CV curves of the 5-nm TiO_2/NiFeS sample with different scanning rates. (d) Scan rate dependence of current density of the 5-nm TiO_2/NiFeS sample at 1.14 V vs. RHE. (e) CV curves of the uncoated NiFeS sample with different scanning rates. (f) Scan rate dependence of current density of the NiFeS sample at 1.14 V vs. RHE.

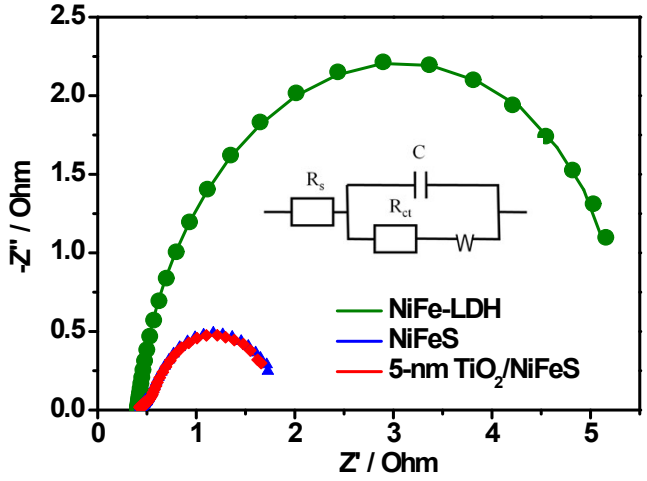

	Solution resistance (R_s), Ω	Charge transfer resistance (R_{ct}), Ω	Capacitance (C), nF·cm^{-2}
NiFe-LDH	0.403	5.249	5.9×10^{-5}
NiFeS	0.455	1.563	4.6×10^{-5}
5-nm TiO_2/NiFeS	0.458	1.526	4.4×10^{-5}

Figure S4. Nyquist plots of NiFe-LDH, NiFeS, and 5-nm ALD TiO_2/NiFeS electrodes held at a cathodic overpotential of -100 mV and the corresponding equivalent circuit. Fitted values are listed in the table. The resistances for NiFeS and 5-nm ALD TiO_2/NiFeS electrodes are small (~ 1 Ω) and comparable, so that the expected improvement in charge-transfer resistance will need to be characterized by more accurate methods in a future study.

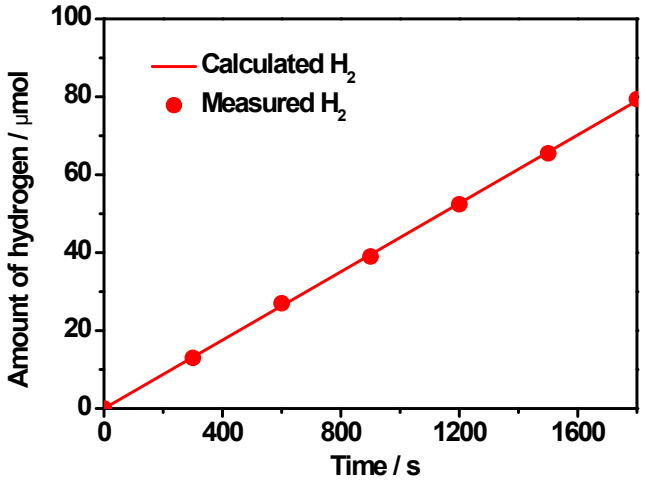

Figure S5. Produced H_2 gas molar quantities as a function of time overlaid with the quantities of evolved H_2 calculated from the amount of charge passed assuming 100% Faradaic efficiency.

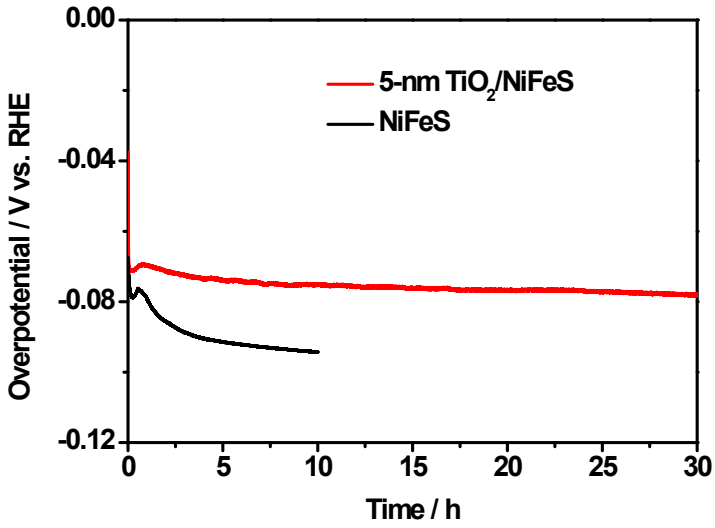

Figure S6. Chronopotentiometry recorded for the 5-nm ALD TiO_2/NiFeS and TiO_2/NiFeS electrodes which are set at a constant current density of -10 mA cm^{-2}.

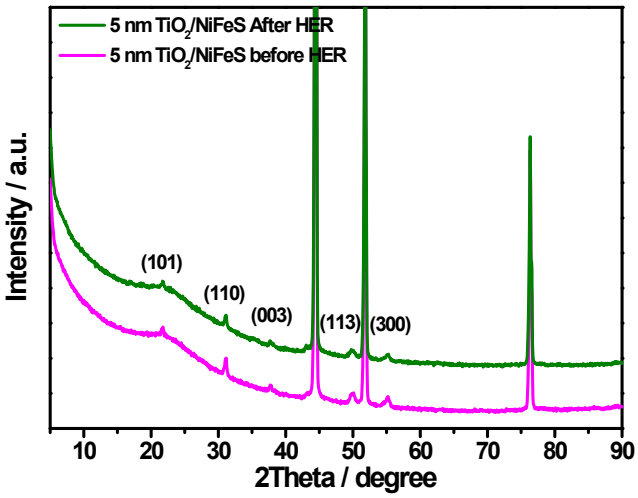

Figure S7. X-ray diffraction (XRD) patterns of 5-nm NiFeS nanosheets before and after 30-h HER operation at -10 mA cm^{-2}.

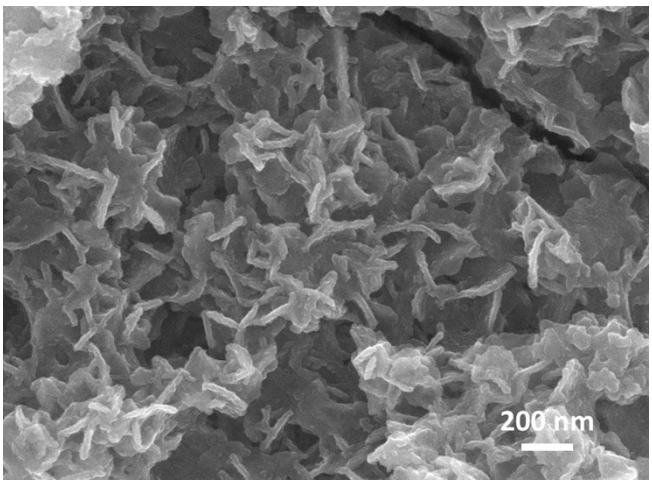

Figure S8. Scanning electron microscope (SEM) image of the 5-nm ALD TiO_2/NiFeS sample after stability test.

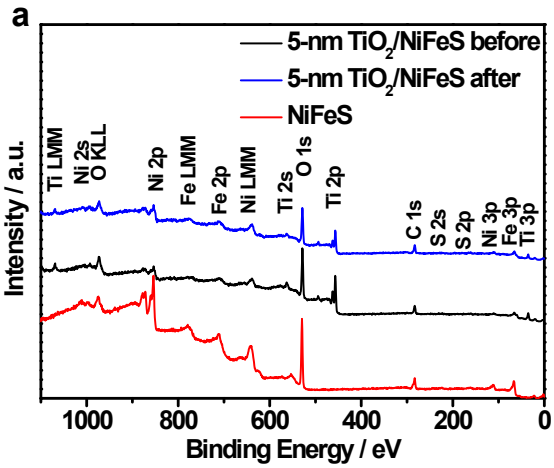
a
5-nm TiO2/NiFeS before
5-nm TiO2/NiFeS after
NiFeS
Ti LMM
Ni 2s
O KLL
Ni 2p
Fe LMM
Fe 2p
Ni LMM
Ti 2s
O 1s
Ti 2p
C 1s
S 2s
S 2p
Ni 3p
Fe 3p
Ti 3p
Intensity / a.u.
1000
800
600
400
200
0
Binding Energy / eV

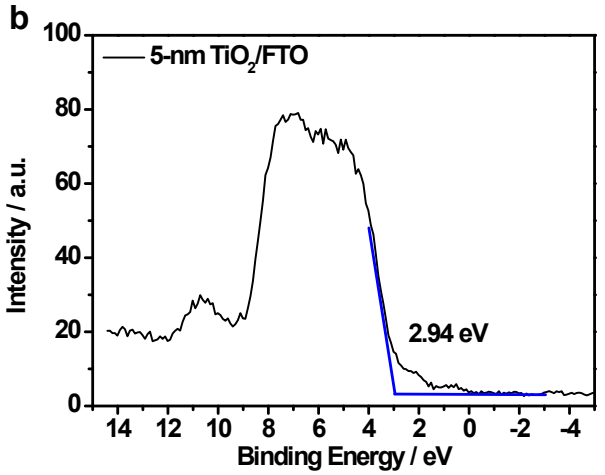
b
5-nm TiO2/FTO
Intensity / a.u.
100
80
60
40
20
0
2.94 eV
14
12
10
8
6
4
2
0
-2
-4
Binding Energy / eV

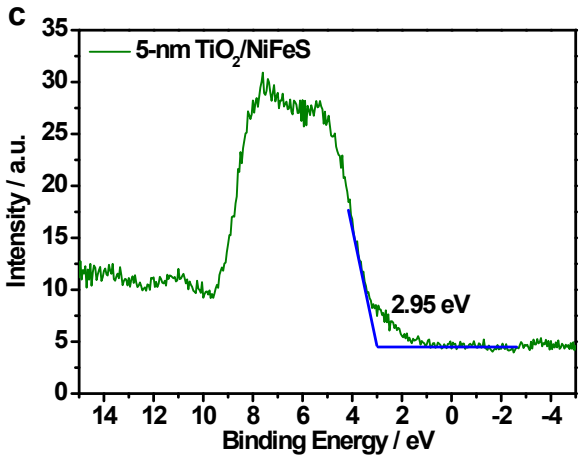
c
5-nm TiO2/NiFeS
Intensity / a.u.
35
30
25
20
15
10
5
0
2.95 eV
14
12
10
8
6
4
2
0
-2
-4
Binding Energy / eV

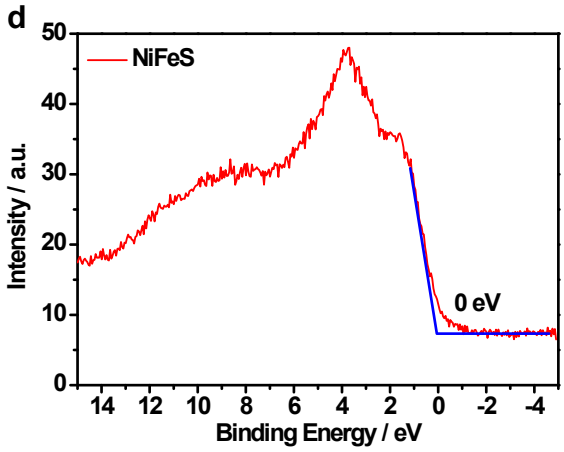

Figure S9. (a) X-ray photoelectron spectroscopy (XPS) survey spectra of the as-synthesized NiFeS samples, 5-nm ALD TiO_2/NiFeS before and after stability test; (b) valence band X-ray photoelectron spectroscopy (VB-XPS) for 5-nm bulk TiO_2 films deposited on FTO substrates; (c) VB-XPS of 5-nm TiO_2/NiFeS sample; and (d) VB-XPS of the as-synthesized NiFeS sample.

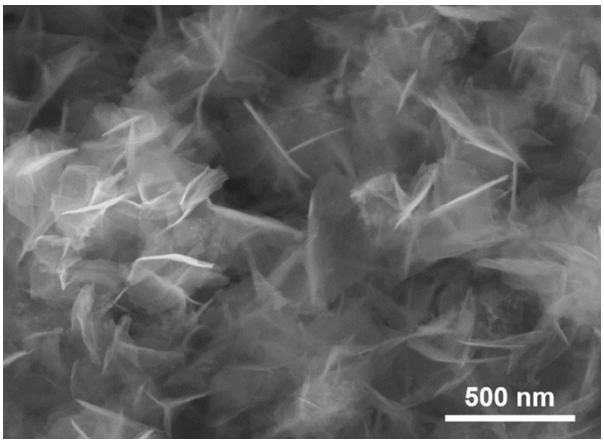

Figure S10. Scanning electron microscope (SEM) image of the as-synthesized NiFe-LDH sample.

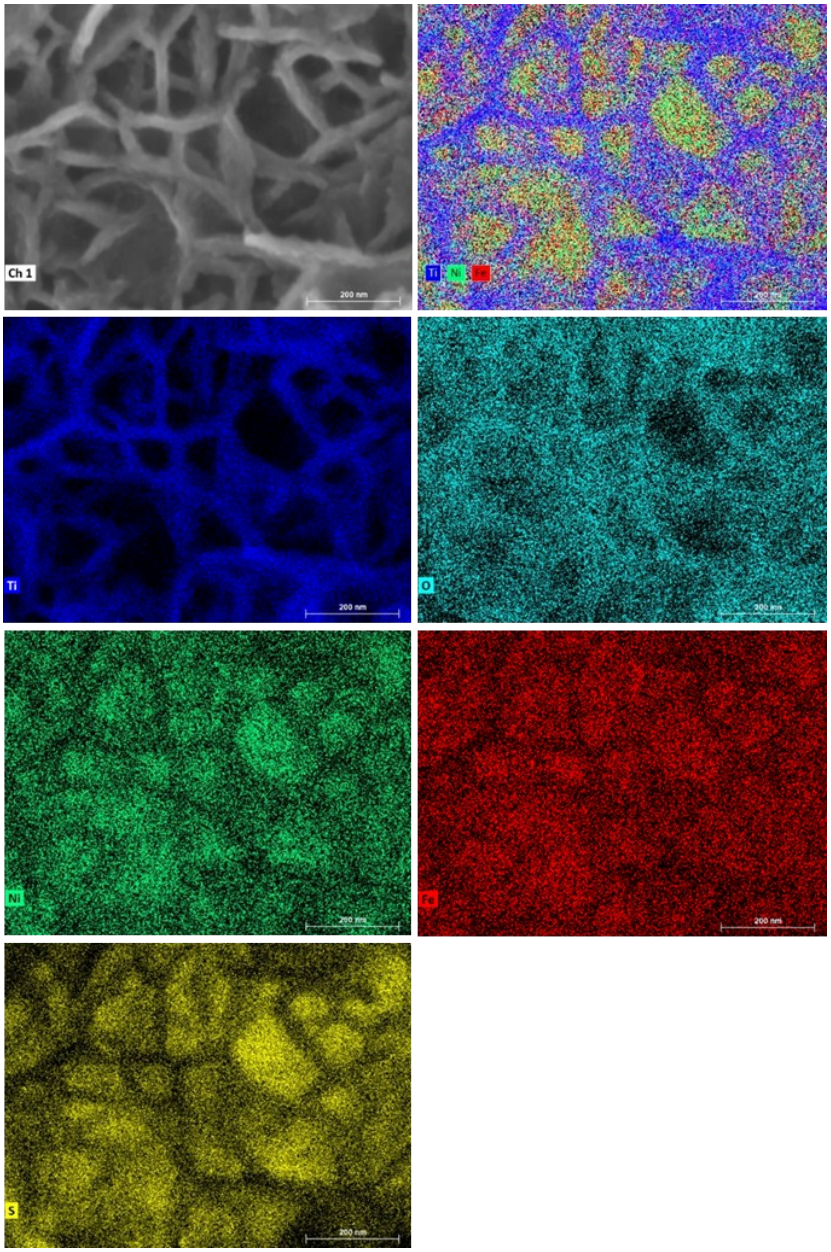

Figure S11. Scanning electron microscope (SEM) image and energy dispersive X-ray spectroscopy (EDX) mapping of the 5-nm ALD TiO_2/NiFeS sample.

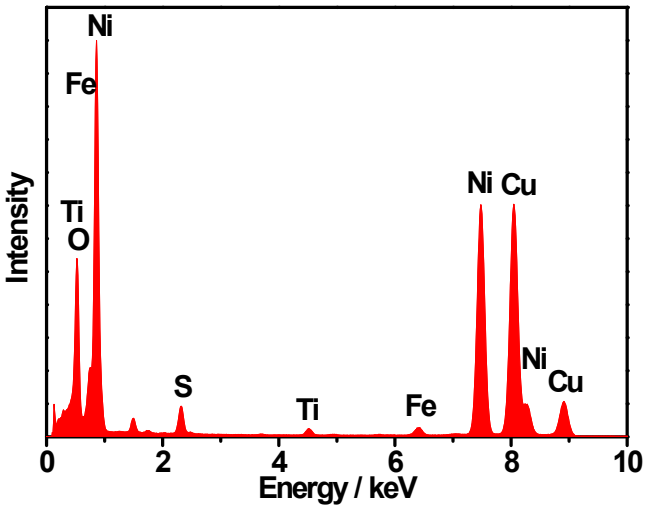

Figure S12. Energy-dispersive X-ray spectroscopy (EDX) analysis of the 5-nm ALD TiO_2/NiFeS sample.

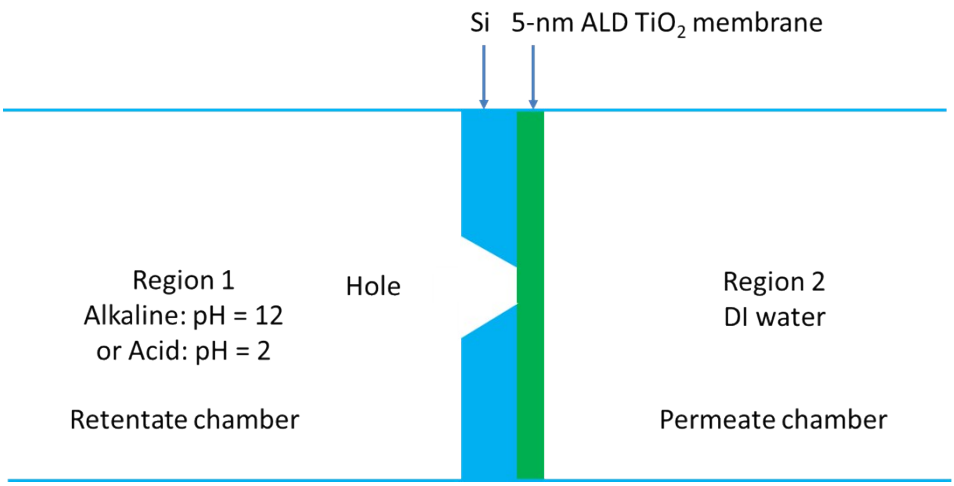

Figure S13. Schematic of H^+ and OH^- permeability test of the 5-nm TiO_2 membrane.

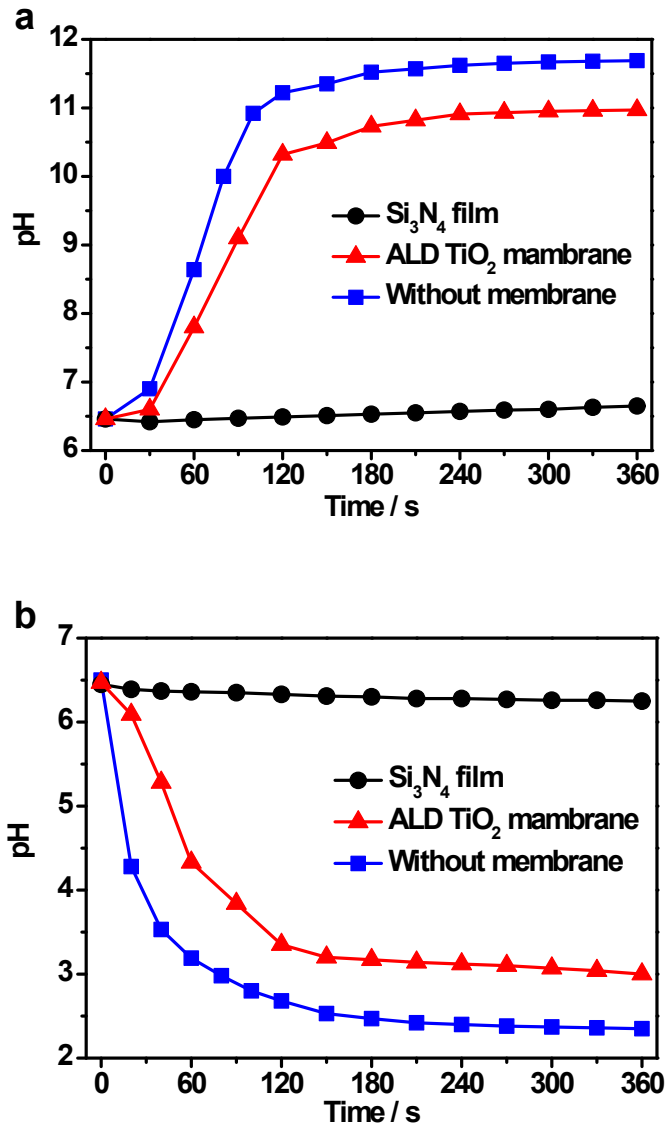

Figure S14. The pH changes in the permeate chamber during the ions permeability test with different membranes (a) in base, and (b) in acid. TiO_2 is permeable to H^+ (or H_3O^+) and OH^- ions, while the Si_3N_4 film is considered impermeable to both species.

Table S1. Comparison of TOFs for hydrogen production.

Samples	TOFs (s^{-1})	Ref.
TiO_2/NiFeS	2.72 (η = 100 mV, 1 M KOH)	This work
NiFeS	0.56 (η = 100 mV, 1 M KOH)	This work
Ni_2P	0.015 (η = 100 mV, 0.5 M H_2SO_4)	9
NiMo	0.05 (η = 100 mV, 2 M KOH)	10
γ-Mo_2N	0.07 (η = 250 mV, 1 M KOH) 0.03 (η = 250 mV, 0.5 M H_2SO_4)	11

Table S2. The inductively coupled plasma-mass spectrometry (ICP-MS) results of the dissolved Ni and Fe ions (mg L^{-1}) (Standard deviation, ± 0.005 mg L^{-1}) after passing the different amount of charge (C) during alkaline hydrogen evolution electrocatalytic reactions.

	54 C		108 C	
	Ni	Fe	Ni	Fe
NiFe-LDH	0.383	0.518	0.651	0.984
NiFeS	0.202	0.310	0.354	0.430
TiO_2/NiFeS	0.081	0.110	0.182	0.193

V. Supplementary References

1. Y. Xue, Z. S. Fishman, J. A. Röhr, Z. Pan, Y. Wang, C. Zhang, S. Zheng, Y. Zhang and S. Hu, *J. Mater. Chem. A*, 2018, **6**, 21918-21926.
2. G. Siddiqi, Z. Luo, Y. Xie, Z. Pan, Q. Zhu, J. A. Röhr, J. J. Cha and S. Hu, *ACS Appl. Mater. Inter.*, 2018, **10**, 18805-18815.
3. F. Lyu, Y. Bai, Z. Li, W. Xu, Q. Wang, J. Mao, L. Wang, X. Zhang and Y. Yin, *Adv. Funct. Mater.*, 2017, **27**, 1702324.
4. C. C. McCrory, S. Jung, I. M. Ferrer, S. M. Chatman, J. C. Peters and T. F. Jaramillo, *J. Am. Chem. Soc.*, 2015, **137**, 4347-4357.
5. P. Ganesan, A. Sivanantham and S. Shanmugam, *J. Mater. Chem. A*, 2016, **4**, 16394-16402.
6. G. Zhang, Y.-S. Feng, W.-T. Lu, D. He, C.-Y. Wang, Y.-K. Li, X.-Y. Wang and F.-F. Cao, *ACS Catal.*, 2018, **8**, 5431-5441.
7. X. Wang, Y. Li, X. Liu, S. Gao, B. Huang and Y. Dai, *Chinese J. Catal.*, 2015, **36**, 389-399.
8. C. Ros, T. Andreu, M. D. Hernández-Alonso, G. Penelas-Pérez, J. Arbiol and J. R. Morante, *ACS Appl. Mater. Inter.*, 2017, **9**, 17932-17941.
9. E. J. Popczun, J. R. McKone, C. G. Read, A. J. Biacchi, A. M. Wiltrout, N. S. Lewis and R. E. Schaak, *J. Am. Chem. Soc.*, 2013, **135**, 9267-9270.
10. J. R. McKone, B. F. Sadtler, C. A. Werlang, N. S. Lewis and H. B. Gray, *ACS Catal.*, 2013, **3**, 166-169.
11. L. Ma, L. R. L. Ting, V. Molinari, C. Giordano and B. S. Yeo, *J. Mater. Chem. A*, 2015, **3**, 8361-8368.